International Journal of Greenhouse Gas Control 107 (2021) 103293

Contents lists available at ScienceDirect

International Journal of Greenhouse Gas Control

journal homepage: www.elsevier.com/locate/ijggc

A model for the fate of carbon dioxide from a simulated carbon storage seep

Scott Loranger [a,b,*], Geir Pedersen [c], Ann E.A. Blomberg [a]

[a] Norwegian Geotechnical Institute, Sognsveien 72, 0855 Oslo, Norway
[b] Woods Hole Oceanographic Institution, 86 Water Street, Woods Hole, MA, USA
[c] Institute of Marine Research, Postboks 1870 Nordnes, NO-5817 Bergen, Norway

ARTICLE INFO

Keywords:
CO2 seep
Carbon capture and storage
Leak detection
Numerical simulation

ABSTRACT

Offshore geological carbon storage (GCS) is a rapidly developing technology essential for meeting international climate goals. While the likelihood of leakage from a properly planned geological sequestration site is low, assurance that CO_2 stays contained will require robust monitoring programs. While seismic imaging methods are used to monitor the geological reservoir, the ideal method for monitoring the water column above the reservoir depends on the fate and transport of CO_2. Whether CO_2 is likely to be present as a rising seep of bubbles or dissolved in the water column near the seafloor will determine the appropriate monitoring technology and lead to a better understanding of the environmental impact of a potential leak. In this study, high definition video of a laboratory release of a carbon dioxide bubble seep recorded the size distribution of bubbles as a function of flow rate and orifice diameter. The transport of CO_2 from different bubble size distributions was then modeled using the Texas A&M Oil Spill Calculator modeling suite. Model results show that the most important factor determining the rise height and transport of CO_2 from the simulated leak was the maximum initial bubble size. For a maximum bubble radius of 5 mm, 95% of CO_2 in the simulated seep reached a height of 17.1 m above the seafloor. When the maximum bubble radius was limited to 3 mm, 95% of CO_2 dissolved by 7.8 m above the seafloor. The modeled results were verified during a controlled release of CO_2 in Oslo Fjord.

ϕ	orifice diameter
$\dot{m}(z)$	total mass flow rate of gaseous CO_2 at depth z
$a(z)$	modeled radius of bubble as at depth z
a_i	initial radius of a bubble
$m_{CO2}(a,z)$	modeled mass of CO_2 in a bubble with radius a at depth z
N	the total number of bubbles released per second
$n(a_i)$da	number of bubbles per unit volume of initial size a_i in bins of width da
$P(a_i)$da	the probability of the release of a bubble of initial radius a_i in bins with width da
Q_{CO2}	volumetric release rate of CO_2
Q_w	volumetric flow rate of surrounding water
r_p	radius of the seep
VF	void fraction
w_{max}	rise rate of the fastest rising bubble in the seep
z	depth

1. Introduction

Carbon capture and storage (CCS), is one of a suite of tools necessary for meeting international climate goals (IPCC, 2014). As of 2019, 19 CCS sites are in operation and 32 sites are under development (Global CCS Institute, 2019). The CCS process involves capturing waste carbon dioxide (CO_2) from industrial sources, such as fossil fuel and cement production, instead of releasing it into the atmosphere. The captured CO_2 is then injected into a suitable storage reservoir for permanent storage. After injection, the CO_2 storage site is monitored to ensure storage integrity, and to detect and quantify any unintended leakage if it should occur.

A 2008 report by the International Energy Agency found that leakage from properly selected geological carbons storage sites (i.e. sites with a confirmed laterally continuous low permeability caprock) is very unlikely, with less than 0.0001 events per 1000 years through the overburden and higher probabilities, up to 0.1 events per 1000 years through well sites (Greenhouse Gas R&D Programme (IEA GHG), 2008). While leakage from offshore geological storage sites is unlikely, monitoring is recommended to verify CO_2 containment. Further, it is important to

* Corresponding author at: Department of Applied Ocean Physics and Engineering, Woods Hole Oceanographic Institution, Woods Hole, MA 02543, USA.
E-mail address: SLoranger@whoi.edu (S. Loranger).

https://doi.org/10.1016/j.ijggc.2021.103293
Received 2 July 2020; Received in revised form 26 January 2021; Accepted 28 February 2021
Available online 11 March 2021

have adequate methods to investigate risk structures or signs of potential leakage, and to be able to quantify leakage in the event that it should occur. A monitoring program should be related to a site-specific risk assessment, and cover the reservoir and overburden, as well as the seabed/water column above the storage formation (Waarum et al., 2017). While monitoring of the reservoir and overburden is generally performed by seismic techniques (Jenkins et al., 2015; Arts et al., 2004) the appropriate methodology for monitoring the water column depends on, among other things, how rapidly CO_2 dissolves in seawater.

CO_2 bubbles dissolve rapidly into the surrounding undersaturated water column, especially compared to other well studied gases associated with marine seeps, such as methane. However, studies of CO_2 bubbles from artificial and natural seeps disagree on the ultimate fate of CO_2 bubbles, with some finding CO_2 is completely dissolved in the first few meters and others finding transport of CO_2 farther into the water column (Gros et al., 2019; Lin et al., 2019; Vielstädte et al., 2019). Whether CO_2 from a leak will be present as dissolved in the water column or in gas phase has significant implications for the spatial extent of a leak as well as the appropriate technology for monitoring the water column. In particular, active acoustic sensors have excellent capabilities for detecting the presence of CO_2 bubbles, while chemical sensors would be better suited to detect the signature of dissolved CO_2.

In this study, we simulated leakage of CO_2 from an offshore storage site and estimated the resulting mass flow of CO_2 into the water column. The aim was to better understand the fate and rise height of CO_2 bubbles under realistic conditions and to inform the appropriate marine monitoring technology while and contributing to a better understanding of the environmental impact of potential leakage. To predict the fate of CO_2 bubbles, a combination of laboratory measurements and computer simulations were performed. Laboratory measurements of the bubble size distribution as a function of flow rate and orifice size informed the Texas A&M Oilspill Calculator (TAMOC, Dissanayake et al., 2018) which modeled the evolution of bubbles as they rose through the water column. The modeled fate of CO_2 bubbles was validated during a controlled release of CO_2 bubbles in the Oslo Fjord as a part of the ACT4Storage project (Blomberg et al., 2021). This manuscript is organized into three parts: (1) laboratory measurements of bubble size distributions, (2) modeling of the fate and transport of CO_2 bubbles and (3) field validation of the modeling results.

2. Laboratory determination of bubble size distribution

2.1. Methods

An artificial bubble seep was generated in a 12 m × 18 m × 6 m freshwater tank at the University of New Hampshire. Bubbles were released from the needle rosette and camera system described by Loranger et al. (2019) with a calibrated pixel size 86 μm. Cylinders of "Bone Dry" CO_2 (99.9% CO_2, 10 ppm by volume O_2), with an initial pressure of 5.8 MPa at 70 °C were connected to a high precision pressure regulator and flow regulator. The flow regulator at the surface was then connected to the needle rosette. Three needles were used in the experiment with diameters (ϕ) of 1.09, 1.75 and 2.60 mm. The pressure regulator maintained a pressure just above the hydrostatic pressure of the tank sufficient to begin flow, while the flow regulator maintained volumetric release rates (Q_{CO2}) of 1.9, 2.8, 3.8 and 4.7 l/min.

An average of 5 min of video was recorded at a frame rate of 39 frames per second for each ϕ and Q_{CO2}. Videos of the bubble seep were analyzed using Matlab image processing software. Individual frames were read into Matlab, converted to gray scale (Fig. 1a) and then the complement of the image was computed. The images were frequently inverted (the complement computed) throughout the processing algorithm as some functions perform best on dark backgrounds and others on light backgrounds. A gray scaled, inverted background image was subtracted from the individual frame to remove any background objects or lighting gradients (Fig. 1b). The background image was taken from video recorded when no bubbles were being released. Holes in the image were then filled using the imfill command and the image was converted to binary with a threshold of 0.5 (Fig. 1c). Holes were again filled and then the image was inverted once more. The Euclidean distance transform was computed using the bwdist function (Fig. 1d), then the Euclidean distance transform was inverted. (Fig. 1e). All minima in the distance transform with a height of less than 2 pixels were removed using the imhmin function. Finally the watershed transform was

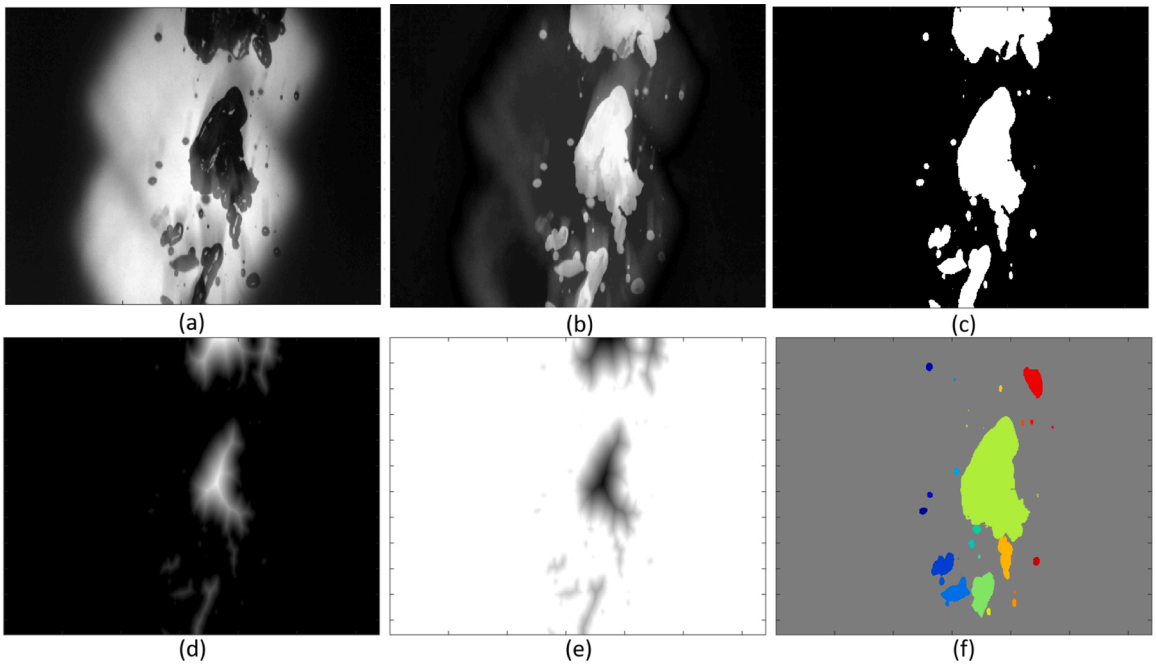

Fig. 1. The image processing work flow showing the steps used to segment frames into individual bubbles. Frames and converted to gray scale (a), the background is removed (b), then the frames are converted to a binary image (c). The Euclidean distance transform is computed on the binary image (c), which is then inverted (d) and a watershed transform is performed on the inverted distance transform (f). The colors in (f) denote individual bubbles.

computed using the watershed function and any bubbles touching the edge of the frame were removed using the imclearboarder function (Fig. 1f).

The initial bubble radius, a_i, was determined from the radius of a circle with an area equal to the area of each bubble. An average of 2.3×10^5 bubbles were detected for each Q_{CO2} and ϕ. To determine the probability, $P(a_i)$da, of a bubble of size a_i being released, the measurements of a_i were binned into 43 μm bins (da = 43 μm). $P(a_i)$da was determined for each Q_{CO2} and ϕ. Bubbles with $a_i > 5$ mm were excluded under the assumption that such large bubbles were either multiple bubbles that were not separated by the image processing methodology, or that such large bubbles would rapidly break into smaller bubbles as they rise. Visual inspection of random bubbles with $a_i > 5$ mm indicated that the former is the most likely scenario. Bubbles larger than 5 mm only account for 3% of all bubbles detected.

The single camera system used in this experiment assumes that bubbles are radially symmetric. Violations of this assumption could cause significant errors to the measurement of an individual bubble, however, it is assumed that the large sample size averaged out any inaccuracies due to non-radially symmetric bubbles. Assuming that the errors due to non-radially symmetric bubbles are random with respect to the plane of the camera, the camera system should provide an accurate estimate of the bubble size distribution.

2.2. Results

The probability of the release of a bubble with initial radius a_i, $P(a_i)$da, was determined for all orifice size (ϕ) and volumetric release rate (Q_{CO2}) combinations; three ϕ's and four Q_{CO2} for a total of twelve $P(a_i)$da's (Fig. 2). To determine if Q_{CO2} had a significant impact on the bubble size distribution, a two-sample Kolmogorov-Smirnov test (KS test) was performed on $P(a_i)$da for the four flow rates at a constant ϕ. The KS test is used to determine if distributions are significantly different, or if the sample distributions are likely to be drawn from the same continuous distribution. When comparing $P(a_i)$da as a function of Q_{CO2} at constant ϕ none of the four $P(a_i)$da were significantly different from one another. The p-value of the KS test determines the significant level at which the distributions are likely to be different, with a p value of one for identical distributions and a p value of 0.05 for distributions that are different at the 95% significance level. The average p-value for all KS tests was >0.5 indicating that the distributions were not significantly different even at the 50% significance level. Therefore, it was determined that the flow rate did not have a significant impact on the bubble size probability function, $P(a_i)$da at constant ϕ.

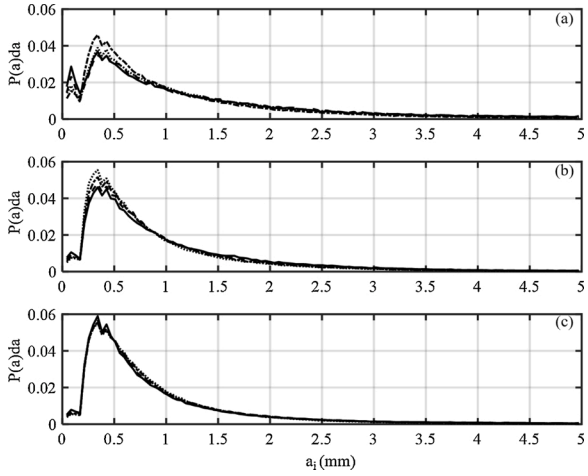

Fig. 2. The probability, $P(a_i)da$, of a bubble being released with initial size a_i, in 43 μm bins when ϕ = 2.60 mm (a), 1.75 mm (b) and 1.09 mm (c). Bubbles were released at Q_{CO2} = 1.9 l/min (solid line), 2.8 l/min (dashed line), 3.8 l/min (dash-dot line), and 4.7 l/min (dotted line). A two-sample Kolmogorov–Smirnov test determined that $P(a_i)da$ for all Q_{CO2} at constant ϕ were drawn from the same continuous distribution.

To determine if ϕ had a significant impact on $P(a_i)$da, all measurements of a_i at each ϕ, regardless of Q_{CO2} were combined to generate three $P(a_i)$da distributions, one for each ϕ (Fig. 3). The three Q_{CO2} independent distributions were then compared using another two-sample KS test. No difference was found between $P(a_i)$da for the two smaller ϕ orifices (p = 0.658). However, both smaller ϕ orifices differed from the largest ϕ at the >99.9% confidence level ($p < 0.001$). The orifice size had a significant impact on $P(a_i)$da when comparing either of the smaller orifices to the largest orifice.

3. Simulated fate and transport of gaseous CO_2

3.1. Methods

$P(a_i)$da determined during the tank experiment was used to inform the Texas A&M Oil Spill Calculator (TAMOC) model. The release of individual bubbles from a depth of 58 m was simulated using an ambient water chemistry profile (Fig. 4) from north of Østøya island in Oslo Fjord, near Horten Norway (the location of the controlled release experiment). The discrete bubble model of the TAMOC model suite simulated the evolution of bubbles as they rose including the expansion with decreasing pressure, dissolution of gases from the bubble into the water column and scavenging of gases from the water column into the bubble (Dissanayake et al., 2018). The change in radius, $a(z)$, shape and chemical composition (mass of CO_2, N_2 and N_2) are simulated as a function of depth until the bubble dissolves. Mass transfer was modeled with the "dirty" bubble mass transfer coefficients under the assumption that surfactants were present in high enough quantities to justify the use of the dirty bubble values. The results of that experiment will be submitted for publication separately. The model was computed over 0.5 s time increments with a diameter of dissolution set to 50 μm. Once a bubble shrunk to $a(z)$ = 50 μm, the bubble became neutrally buoyant and dissolved away in the same depth bin that the 50 μm bubble reached. Because of the relatively low Q_{CO2} in this experiment it was assumed that plume effects (entrainment of seawater, turbulence, etc.) were negligible and therefore the seep can be modeled as the sum of the individually modeled bubbles. For higher flow rates, plume effects are likely to be more significant and the stratified plume and bent plume modules of the TAMOC model would be more appropriate for simulating the fate and transport of CO_2 bubbles.

The mass flow rate of gaseous CO_2 in the seep as a function of depth, $\dot{m}(z)$ was modeled as

$$\dot{m}(z) = \int_z^{z+\Delta z} \left[\int_{a_{\min}}^{a_{\max}} m_{CO2}(a,z) \mathrm{N}\ P(a_i)\mathrm{da} \right] \mathrm{dz}, \tag{1}$$

where Δz is the width of the depth bin, $a_{\min}$ and $a_{\max}$ are the minimum and maximum radii in the distribution and $m_{CO2}(a,z)$ is the mass of CO_2 from a single bubble of radius a as a function of depth determined from the TAMOC model. $P(a_i)$da is the probability distribution determined from the laboratory measurements and N is the total number of bubbles released per unit time. N can be determined by evaluating the void fraction, VF,

$$\mathrm{VF} = \frac{Q_{CO2}}{Q_w}, \tag{2}$$

where Q is volumetric flow rate, and the subscripts CO2 and w indicate CO_2 and water. The volumetric flow rate of water, Q_w, was determined from

$$Q_w = \pi r_p^2 w_{\max}, \tag{3}$$

where r_p is the radius of the seep and $w_{\max}$ is the rise rate of the fastest

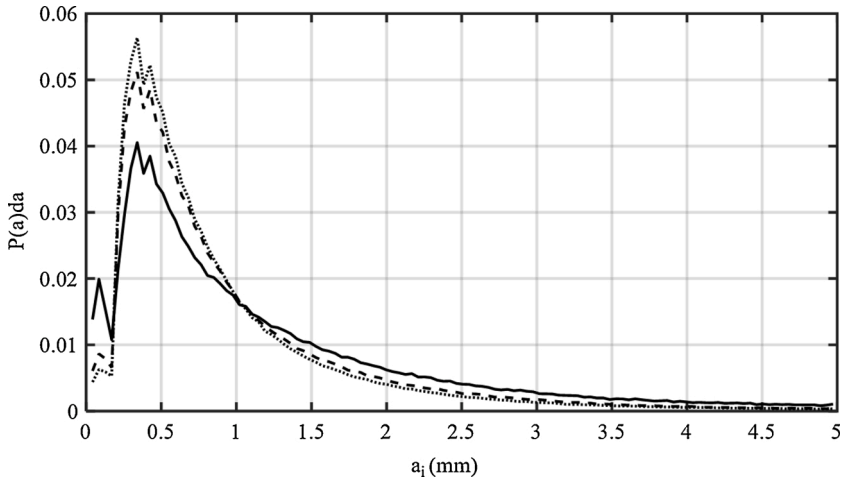

Fig. 3. The probability, $P(a_i)da$, of a bubble being released with initial size a_i, in 43 μm bins when ϕ = 2.60 mm (solid line), 1.75 mm (dashed line) and 1.09 mm (dotted line) when measurements from all flow rates were combined. The two-sample Kolmogorov-Smirnov test determined that the smaller ϕ distributions were not significantly different, while the largest ϕ distribution is significantly different from the other two distributions at the >99.9% confidence interval.

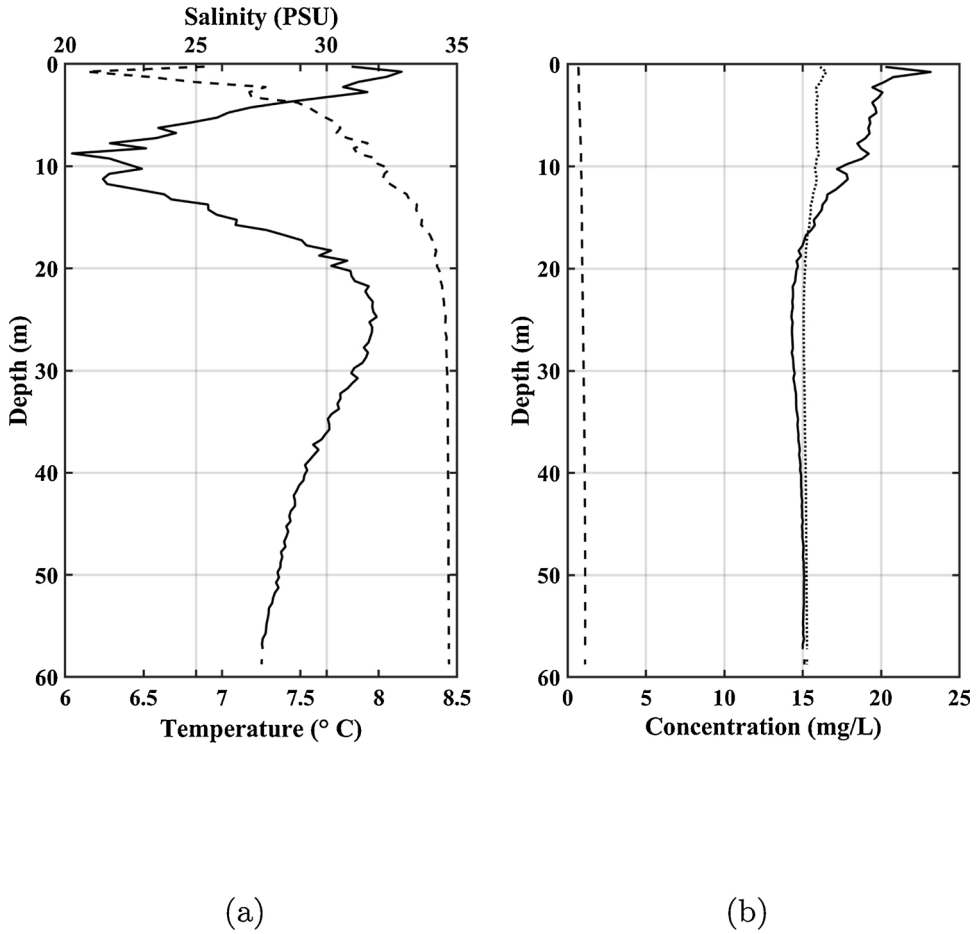

Fig. 4. Temperature (a, solid line) and salinity (a, dashed line) and *DO* (b, solid line), CO_2 (b, dashed line) and N_2 (b, dotted line) in the water column.

rising bubble. Q_{CO2} is the volumetric flow rate measured by the flow regulator in units of m^3/s. VF can also be expressed as,

$$\mathrm{VF} = \frac{4\pi}{3}\int_{a_{\min}}^{a_{\max}} a_i^3 n(a_i)\mathrm{da}, \tag{4}$$

where $n(a_i)$da is the number of bubbles of size a_i per unit volume in each bin. $n(a_i)$da is related to $P(a_i)$da by,

$$n(a_i)\mathrm{da} = \frac{\mathrm{N}\ \mathrm{P}(a_i)\mathrm{da}}{Q_w}. \tag{5}$$

Combining Eqs. (2), (4) and (5)

$$N = \frac{3Q_{CO2}}{4\pi}\frac{1}{\int_{a_{\min}}^{a_{\max}} a_i^3 P(a_i)\mathrm{da}}. \tag{6}$$

N was therefore determined from the measurements of the initial bubble size (a_i) and probability distribution $P(a_i)$da measured by the camera system. N and $P(a_i)$da were then combined with the mass of a bubble at depth z from the TAMOC model, $m_{CO2}(a, z)$ to determine the total mass flow of gaseous CO_2 in a depth bin, $\dot{m}(z)$.

3.2. Results

Two significantly different bubble size probability distributions, $P(a_i)$da, were used to model the mass transport of CO_2 in the bubble seep; $P(a_i)$da from the smallest ϕ and from the largest ϕ (dotted and solid lines in Fig. 3). The number of bubbles per unit volume at the release point, $n(a_i)$da, was determined for the two distributions at four flow rates, Q_{CO2}, according to Eqs. (5) and (6) for a seep with $r_p = 1$ m (Fig. 5). The VFs are listed in Table 1. $n(a_i)$da resulting from the largest ϕ (Fig. 5a) had a flatter distribution, while the smallest ϕ had the steeper slope (Fig. 5c) with a higher peak at small a_i ($a_i < 1$ mm). While the slope of $n(a_i)$da varied by ϕ, the number of large bubbles ($a_i > 2$ mm) was relatively constant between the two distributions at the same flow rate.

Eq. (1) was used to determine $\dot{m}(z)$, the total mass flow of gaseous CO_2 in the seep as a function of depth in 0.1 m depth bins. Fig. 6 shows the resulting $\dot{m}(z)$ for the different $P(a_i)$da and Q_{CO2}.

As carbon dioxide is dissolved from the bubble into the surrounding water, dissolved gasses present in the water column are simultaneously scavenged from the surrounding water into the bubble (Socolofsky et al., 2015). Fig. 7a shows $\dot{m}(z)$ of the three gasses used in this simulation (CO_2, N_2, and O_2) as well as $\dot{m}(z)$ of all gases combined. At about 30 m above the seafloor the bubble is no longer dominated by CO_2 and N_2 and O_2 dominate. CO_2 in the simulated seep dissolves slowly with depth until about 25 m above the seafloor where the bubbles dissolve quickly as a function of depth.

The camera system used in the laboratory experiment measures bubble size immediately above the orifice at the release point of the seep. While bubbles up to $a_i = 5$ mm may be present at the release point, it is likely that these bubbles are unstable and would break into smaller bubbles as they rise in the water column. Other studies indicate a maximum radius of $a_i = 3$ mm (Vielstädte et al., 2019; Gros et al., 2019; Lin et al., 2019). Simulations were re-run with maximum $a_i = 3$ mm under the assumption that the larger bubbles break up to be evenly distributed across all bubble sizes less than 3 mm (Fig. 7b). For this case no bubbles reach the surface and the seep only reaches a depth of 12 m.

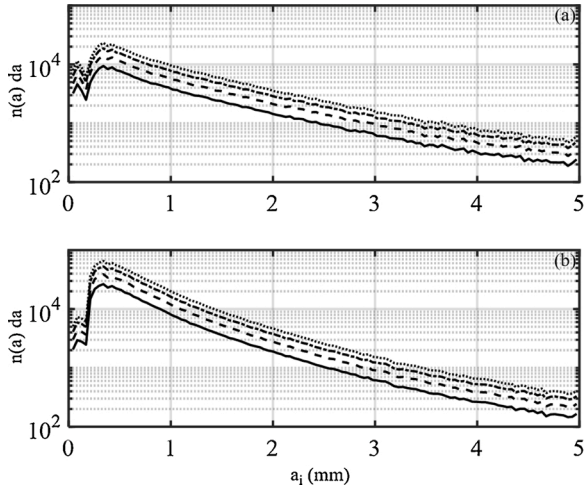

Fig. 5. The number of bubbles of initial size a_i per unit volume ($n(a_i)da$) in 43 µm bins for bubbles released when $\phi = 2.60$ mm (a) and 1.09 mm (b). $n(a_i)$ da was determined for $Q_{CO2} = 1.9$ l/min (solid line), 2.8 l/min (dashed line), 3.8 l/min (dash-dot line), and 4.7 l/min (dotted line).

Table 1
The void fraction, *VF*, for all flow rates.

Flow rate (l/min)	Void fraction
1.9	6.44×10^{-3}
2.8	9.49×10^{-3}
3.8	12.9×10^{-3}
4.7	15.9×10^{-3}

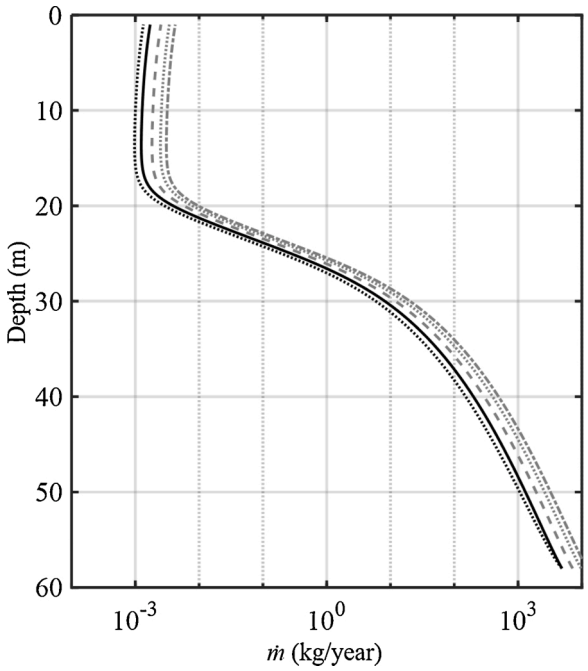

Fig. 6. The mass flow rate, $\dot{m}$ of CO_2 in the seep for $Q_{CO2} = 1.9$ l/min and $\phi = 1.09$ mm(dotted black line) and $\phi = 2.60$ mm (solid black line) in 0.1 m depth bins. The gray lines show the increase in $\dot{m}$ with Q_{CO2} (2.8 l/min (dashed gray line), 3.8 l/min (dotted gray line), and 4.7 l/min (dash-dot gray line), $\phi = 2.60$ mm).

Fig. 8 shows the maximum height reached by a seep as a function of the maximum bubble size.

4. Model validation based on a field experiment

4.1. Methods

The simulated fate and transport of CO_2 bubbles was validated during a controlled release experiment in the Oslo Fjord in May, 2019. 99.99% pure CO_2 bubbles were released from a seep generating device placed at the seabed at a water depth of 58 m. Bubbles were released from five 3 mm diameter orifices at a flow rate of 1.33 l/min. Further details on the controlled release experiment can be found here (Blomberg et al., 2021).

The rise height of the bubble plume emanating from the seep generating device was quantified by a multibeam echo sounder (MBES, Kongsberg EM2040) mounted on the hull of the R/V Simrad Echo. Five passes over the seep, where the seep was in the center beams of the MBES, were performed.

EM2040 MBES.all files were processed using the water column processing algorithms for Kongsberg sonars in the Ifremer SonarScope Software (Augustin, 2019). For each MBES file a water column polar echogram (depth, across distance) and a 3D matrix (depth, across distance, ping number) dataset was produced, following the recommended procedures in the SonarScope manual. From the 3D matrices along track

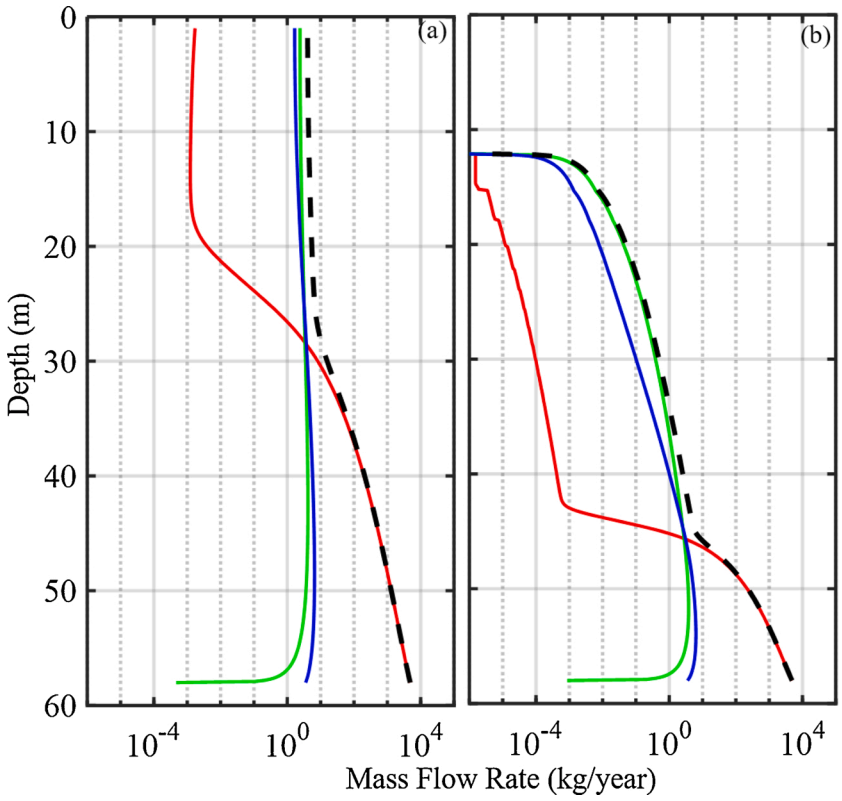

Fig. 7. The $\dot{m}$ of the component gases (CO_2 (red), N_2 (blue), and O_2 (green)) in the seep where the maximum $a_i = 5$ mm (a) and $a_i = 3$ mm (b) in 0.1 m depth bins. $\dot{m}(z)$ is shown here for a release from $\phi = 2.60$ mm where $Q_{CO2} = 1.9$ l/min. The dashed black line shows $\dot{m}(z)$ of all gases combined.

slices were exported and further processed in Matlab, where for each pass of the plume the slices covering the plume were merged and a 3×3 averaging filter was applied. Backscatter by the plume dropping lower than 3 dB above the background backscatter was used as estimated top of the plume as observed by the MBES for each pass. This estimated is likely a conservative estimate of the actual plume height, based on visual inspection of the slices.

4.2. Results

On the five passes over the seep where the seep was in the center beams of the MBES the seep reached an average depth of 22.9 m with a standard deviation of 2.9 m (Fig. 9). The 37.1 m tall seep corresponds to a maximum bubble radius of 2.8 mm with a standard deviation of 0.1 mm.

5. Discussion

It was found that the bubble size probability distribution, $P(a_i)$da, was independent of flow rate, Q_{CO2}, indicating that as Q_{CO2} increases more bubbles are released, but the distribution stays the same (Fig. 2). This observation lends credence to the assumption that the seep generated by the relatively low Q_{CO2} in this experiment behaved as the sum of the individually modeled bubbles and that no seep effects (turbulence, entertainment of water, etc.) needed to be considered (Wang et al., 2019). For higher flows were plume effects, especially turbulence induced shear, are likely to be more pronounced, a relationship between flow rate and initial bubble size distribution is likely to be significant.

While $P(a_i)$da was independent of Q_{CO2}, there was a significant difference between $P(a_i)$da from the largest ϕ compared to the two smaller ϕ (Fig. 3). While the KS test revealed no significant difference between $P(a_i)$da for the two smaller ϕ orifices it is possible that the change to $P(a_i)$da was too subtle for the resolution of the camera system to detect. The distributions were not significantly different, however the peak in $P(a_i)$da at smaller bubble sizes does show a trend of decreasing with increasing ϕ, which may have been significant with finer resolution a_i bins.

However, the significant difference between $P(a_i)$da for the largest ϕ and smallest ϕ did not translate to a large difference in the mass flow rate of CO_2 in the seep, $\dot{m}(z)$ (Fig. 6). While the ϕ influenced the number of small bubbles per unit volume, $n(a_i)$da, the total number of large bubbles ($a_i > 2$ mm) was relatively constant between the different distributions (Fig. 5). $\dot{m}$ is dominated by the largest bubbles, where the volume (and therefore the mass at a given depth where the density is constant) scales with the cube of the radius.

The most important factor contributing to the terminal height of a seafloor sourced CO_2 seeps is the maximum initial bubble size, a_i. In this experiment the maximum measured bubble initial radius, a_i, was 5 . Bubbles larger than 5 mm are likely to be unstable beyond the initial release point – where the measurement was made – and will therefor likely break into smaller bubbles. Other experiments on both natural and simulated CO_2 seeps found that the maximum a_i was around 3 mm (Lin et al., 2019; Gros et al., 2019; Vielstädte et al., 2019). Seeps that contain bubbles with $a_i > 3$ mm would reach the surface in this simulation and water depth (58 m) while seeps comprised of bubbles with $a_i < 3$ mm would not reach the surface, and the transport of CO_2 would be contained to shallower depths (Fig. 8). If 5 mm was the largest a_i, 50% of the CO_2 in the seep dissolved by 4.1 m and 95% of the CO_2 in the seep dissolved by 17.1 m above the seafloor. Whereas for a maximum a_i of 3 mm, 50% of CO_2 dissolved by 2.1 m above the seafloor and 95% of CO_2 dissolved by 7.8 m.

This study predicts that in realistic conditions similar to those modeled here, a seep of CO_2 bubbles will be present and the bubbles will persist tens of meters above the seafloor, depending on the maximum bubble size, as predicted by the model and as seen during the simulated CO_2 releases experiment. The model predicts that the majority of CO_2

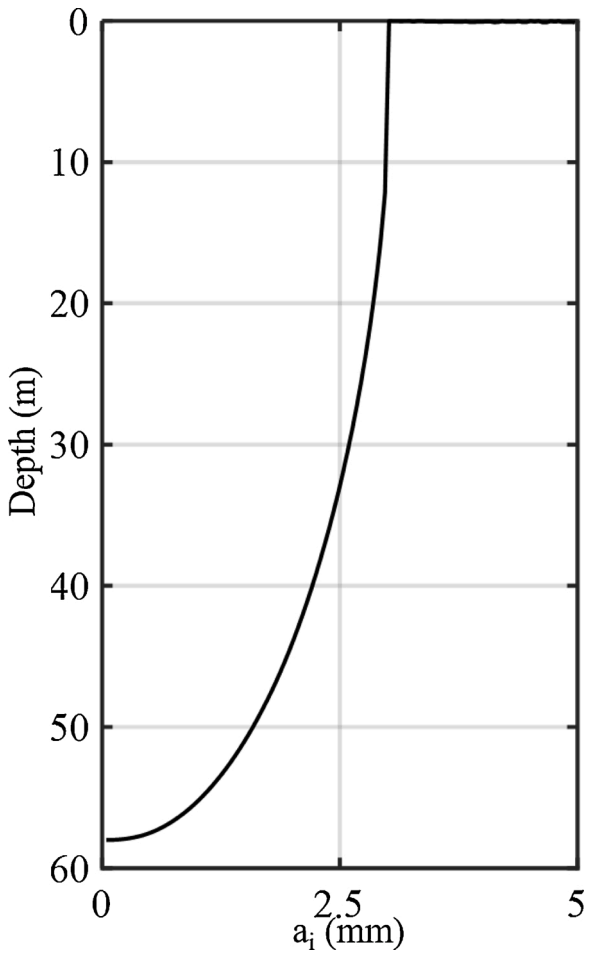

Fig. 8. The maximum height reached by a bubble by the initial radius of the bubble, a_i. Bubbles with $a_i = 3$ mm will rise to a depth of 12 m. Bubbles where $a_i > 3$ mm rise to the surface in this simulation.

will be dissolved at greater depths than the maximum height reached by the bubble due to the rapid dissolution of CO_2 in seawater. As the bubble rises and CO_2 dissolves, the model predicts that other gases, namely N_2 and O_2, are scavenged from the water column into the bubble. It is this scavenging process that allows the bubble to persist and reach a greater height than predicted if considering CO_2 alone. While the bubbles higher in the water column no longer contain CO_2 they do provide a strongly scattering acoustic target which is easily detectable using active acoustic sensors.

When determining the appropriate instrumentation for an offshore geological carbon storage site, an important factor is how high into the water column the presence of bubbles is expected. This again is directly related to the assumed bubble size distribution, and importantly the maximum bubble size of a potential CO_2. If potential bubble seeps are limited to a meter or two above the sea floor, chemical sensors near the seabed and close to likely release points would likely be the preferred instrumentation while acoustic sensors would be of limited use. On the other hand, if bubbles can be expected to rise higher into the water column, acoustic instrumentation would provide a more efficient means of marine monitoring. A column of bubbles provides a clear and distinct acoustic target, as can be seen in the MBES data (Fig. 9. Acoustic monitoring systems can be deployed on manned or un-manned surface vessels as well as underwater vehicles (AUVs, ROVs, UUVs). Acoustic sensors also provide significantly higher detection ranges as compared to chemical sensors with relatively short detection ranges.

Accurately predicting the transport of CO_2 from a the seabed is not only important for determining the appropriate monitoring technology, but also for predicting the impact of a potential release of CO_2 from a sequestration site. Finally, local conditions such as water depth and chemistry, should be considered when modeling a leak using the methodology in this study.

The bubble plume modeling of subsea releases of CO_2 presented in this paper is an enabler for quantitative active acoustic measurements of mass flow rates. With a calibrated sonar it would be possible to acoustically quantify a CO_2 plume using acoustic scattering models in a manner similar to that described by Loranger and Weber (2020). Calibrated split-beam echo sounders typically have improved dynamic range compared to MBES, and could also provide a more accurate identification of the maximum height reached by the seep.

6. Conclusions

In this study, the Texas A&M Oil Spill Calculator (TAMOC) discrete bubble model was used to predict the fate of CO_2 released from the seafloor. Modeled results were validated using MBES data acquired during a controlled CO_2 release experiment. The bubble size distribution for CO_2 bubbles was measured in the laboratory as a function of orifice size and flow rate, where it was determined that the orifice size had a significant impact on size distribution while flow rate did not, for the orifice sizes and flow rates measured in this experiment. The size distributions measured in the laboratory were then used to inform the TAMOC model and predict the mass flow rate of CO_2 in a simulated seep. While orifice size resulted in significantly different size distribution, the total number of large ($a_i > 2.0$ mm) bubbles was constant across orifice sizes. The largest bubbles drive the mass flow rate in the seep and flow rate did not vary significantly across the size distributions in this study. The maximum bubble size is the dominant contributor to the total rise height of a CO_2 bubble seep, with bubbles greater than a_i predicted to reach the surface in a release from 58 m depth. While seeps may reach heights of tens of meters above the seafloor, dependent on the maximum bubble size in the seep, the majority of CO_2 dissolves into the water column much shallower than the maximum rise height of the seep. A field experiment performed in Oslo Fjord found that a controlled release of CO_2 generated a seep acoustically detected to rise almost 40 m above the seafloor, consistent with the predicted height of a seep with a maximum bubble radius of 2.8 mm.

CRediT authorship contribution statement

Scott Loranger: conceptualization, methodology, software, formal analysis, investigation, writing - original draft, visualization. Geir Pedersen: conceptualization, methodology, formal analysis, writing – original draft, visualization. Ann E.A. Blomberg: conceptualization, methodology, investigation, writing – original draft, supervision. project administration.

Acknowledgements

The authors kindly thank Espen Eek, Christian Totland and Ivar-Kristian Waarum at the Norwegian Geotechnical Institute for scientific input to this paper. We also thank Frank Reier Knudsen of Kongsberg Maritime for his contributions during data acquisition, processing and analysis. The authors would also like to thank Scott Socolofsky from the University of Texas A&M. This work was carried out as part of the ACT4storage project (617334) funded by Gassnova and Norwegian industry partners through the CLIMIT programme.

Declaration of Competing Interest

The authors declare that they have no known competing financial interests or personal relationships that could have appeared to influence the work reported in this paper.

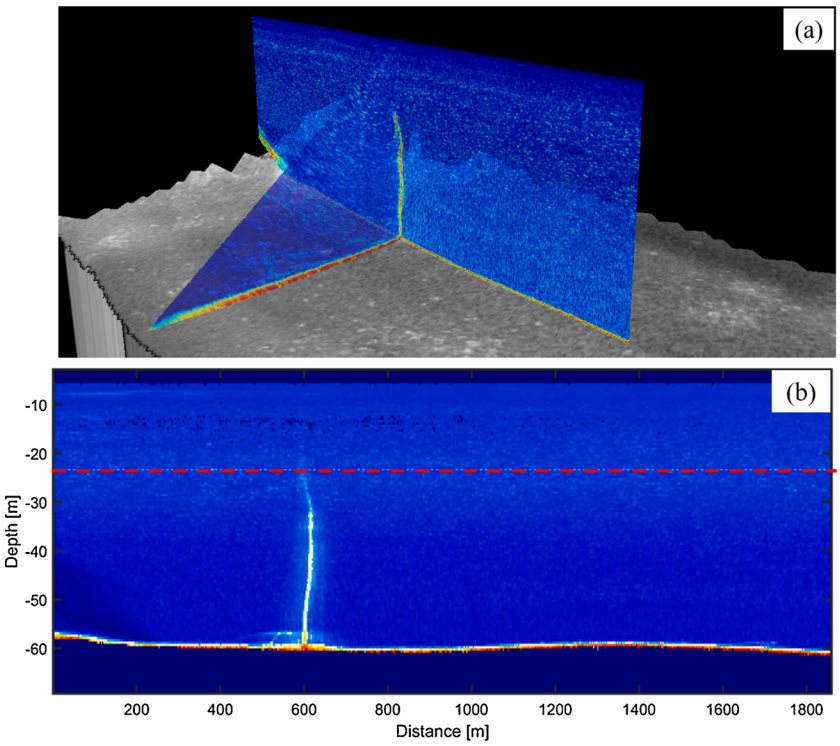

Fig. 9. (a) A composite of a long track slice and polar echogram for a single pass over the seep, showing the plume in both dimensions. (b) Merged and averaged along track slices showing the plume at approximately 600 m distance and the estimated maximum plume height (horizontal dashed red line).

Appendix A. Supplementary data

Supplementary data associated with this article can be found, in the online version, at https://doi.org/10.1016/j.ijggc.2021.103293.

References

Arts, R., Eiken, O., Chadwick, A., Zweigel, P., van der Meer, L., Zinszner, B., 2004. Monitoring of CO2 injected at Sleipner using time-lapse seismic data. Energy 29 (9–10), 1383–1392.

Augustin, J.M., 2019. SonarScope Software On-line. https://www.flotteoceanographique.fr/en/Facilities/Shipboard-software/Analyse-et-traitement-de-l-information/SonarScope.

Blomberg, A.E., Waarum, I.K., Eek, E., Totland, C., Pedersen, G., Lorentzen, O., Loranger, S., 2021. Controlled CO2 Release Experiment, 2019. Tech. Rep. Norwegian Geotechnical Institute.

Dissanayake, A.L., Gros, J., Socolofsky, S.A., 2018. Integral models for bubble, droplet, and multiphase plume dynamics in stratification and crossflow. Environ. Fluid Mech. 18 (5), 1167–1202.

Global CC Institute, 2019. The Global Status of CCS: 2019. Tech. Rep. Global CCS Institute, Australia.

Gros, J., Schmidt, M., Dale, A.W., Linke, P., Vielstädte, L., Bigalke, N., Haeckel, M., Wallmann, K., Sommer, S., 2019. Simulating and quantifying multiple natural subsea CO2 seeps at Panarea Island (Aeolian Islands, Italy) as a proxy for potential leakage from subseabed carbon storage sites. Environ. Sci. Technol. 53 (17), 10258–10268.

Greenhouse Gas R&D Programme (IEA GHG), 2008. Assessment of Sub Sea Ecosystem Impacts, pp. 1–266.

IPCC, 2014. Climate Change 2014: Synthesis Report. Contribution of Working Groups I, II and III to the Fifth Assessment Report of the Intergovernmental Panel on Climate Change. Tech. Rep. Geneva, Switzerland.

Jenkins, C., Chadwick, A., Hovorka, S.D., 2015. The state of the art in monitoring and verification – ten years on. Int. J. Greenhouse Gas Control 40, 312–349.

Lin, Y.S., Lui, H.K., Lee, J., Chen, C.T.A., Burr, G.S., Chou, W.C., Kuo, F.W., 2019. Fates of vent CO2 and its impact on carbonate chemistry in the shallow-water hydrothermal field offshore Kueishantao Islet, NE Taiwan. Mar. Chem. 210, 1–12.

Loranger, S., Pedersen, G., Weber, T.C., 2019. Broadband acoustic scattering from oblate hydrocarbon droplets. J. Acoust. Soc. Am. 146 (2), 1176–1188.

Loranger, S., Weber, T.C., 2020. Shipboard acoustic observations of flow rate from a seafloor sourced oil spill. J. Geophys. Res.: Oceans 125 (10).

Socolofsky, S.A., Dissanayake, A.L., Jun, I., Gros, J., Arey, J.S., Reddy, C.M., 2015. Texas A&M Oilspill Calculator (TAMOC): modeling suite for subsea spills. In: Proceedings from Arctic Marine Oil Pollution Technical Seminar on Environmental Contamination and Response. British Columbia, Canada.

Vielstädte, L., Linke, P., Schmidt, M., Sommer, S., Haeckel, M., Braack, M., Wallmann, K., 2019. Footprint and detectability of a well leaking CO2 in the Central North Sea: implications from a field experiment and numerical modelling. Int. J. Greenhouse Gas Control 84, 190–203.

Waarum, I.K., Blomberg, A.E., Eek, E., Brown, J., Ulfsnes, A., Carpenter, M., Grimsrud, T. S., Park, J., Cornelissen, G., Sparrevik, P., 2017. CCS leakage detection technology – industry needs, government regulations, and sensor performance. Energy Proc. 114 (November 2016), 3613–3627.

Wang, B., Lai, C.C., Socolofsky, S.A., 2019. Mean velocity, spreading and entrainment characteristics of weak bubble plumes in unstratified and stationary water. J. Fluid Mech. 874, 102–130.